ACS Partner Journal
CHEM & BIO ENGINEERING

pubs.acs.org/ChemBioEng
Article

Optimizing Nitrate Electroreduction toward Nearly 100% Ammonia Selectivity through Synergistic RuCu Catalysts and Integrated Coupled Anodic Reaction for High-Value Products

Shuyi Shen,[§] Shuyue Wang,[§] Bo Zhang, Xuesong Zhao, Chen Sun, Shaodong Zhou,* Zhongjian Li, Yang Hou, Lecheng Lei, and Bin Yang*

Cite This: *Chem Bio Eng.* 2025, 2, 41−52

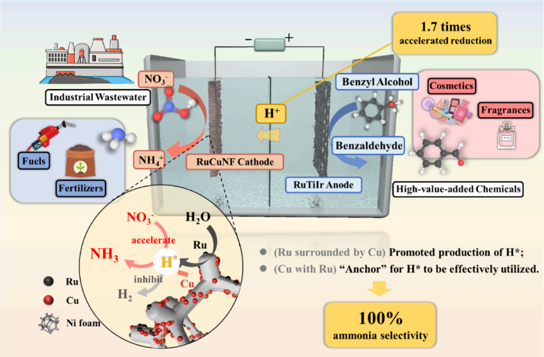

ABSTRACT: Copper-based catalysts have been widely used in the field of the nitrate reduction reaction (NO_3RR) to ammonia, demonstrating high nitrate reduction rates. However, their low selectivity for ammonia production poses significant limitations in practical applications. In this study, we present that the incorporation of Ru into the Cu@Ni foam can achieve nearly 100% selectivity for NH_3 and a high faradaic efficiency of 96.8% in the NO_3RR. Ru not only facilitates the generation of adsorbed hydrogen but also suppresses the HER reaction. This can be attributed to the unique electron distribution exhibited by Ru atoms when surrounded by Cu, leading to a decreased electron-accepting capability. Consequently, this reduction results in a diminished Lewis acidity and a decreased H* adsorption. Importantly, it was confirmed that the incorporation of Cu with Ru serves as "anchor" for atomic H* generated from Ru, inhibiting HER and ensuring the availability of H* for subsequent ammonia production. The synergistic effect between Ru and Cu enhanced the efficiency and selectivity of reduction of nitrate to NH_3. Remarkably, substituting oxygen evolution reaction (OER) with a coupled anodic reaction for the oxidation of benzyl alcohol to benzaldehyde can significantly accelerate the nitrate reduction rate by 1.7 times and achieves a 90% benzaldehyde conversion rate. This research not only introduces innovative strategies for designing high-performance ammonia-selective electrocatalysts but also highlights the potential industrial applications for the synthesis of high-value products.

KEYWORDS: *Electroreduction process, Ru-anchored catalyst, Nitrate reduction reaction, Value-added chemicals, Electrodeposition technique*

1. INTRODUCTION

Ammonia plays a pivotal dual role in various industrial and domestic applications, serving as an indispensable component in the production of agricultural fertilizers and chemicals, while also emerging as a clean and green liquid fuel.[1−3] However, the traditional Haber−Bosch process, which dominates the current production of NH_3 is highly energy-intensive, requiring high temperatures (300−500 °C) and pressures (15−35 MPa).[4,5] In contrast, nitrate, a pervasive pollutant in groundwater resulting from fossil fuel combustion, excessive use of nitrogen-rich fertilizers, and the release of domestic and industrial wastewater,[6] poses significant health and the environmental risks.[7] Recognizing this challenge, the nitrate reduction reaction (NO_3RR) emerges as a promising avenue to produce ammonia, effectively transforming a pollutant into a valuable resource and fostering a greener energy solution. This paradigm shift aligns with the vision of a nitrogen circular economy, bridging the gap between environmental stewardship and energy demands. Despite its potential, the NO_3RR for ammonia production faces several bottleneck issues. First, enhancing the selectivity and catalytic efficiency of catalyst materials remains a critical challenge. Nitrate reduction to ammonia relies on the generation of active hydrogen species (H*) via water splitting. Conversely, if a surplus of hydrogen is not promptly utilized, it tends to favor the hydrogen evolution reaction (HER), thereby compromising the overall selectivity of the catalyst.[8,9]

In recent decades, substantial research efforts have been directed toward the electrochemical reduction of nitrates in aqueous media, utilizing various single transition metal electrodes as catalysts.[8,10−21] Among these, Cu stands out as

Received: July 21, 2024
Revised: October 25, 2024
Accepted: October 27, 2024
Published: November 1, 2024

https://doi.org/10.1021/cbe.4c00124
Chem Bio Eng. 2025, 2, 41−52

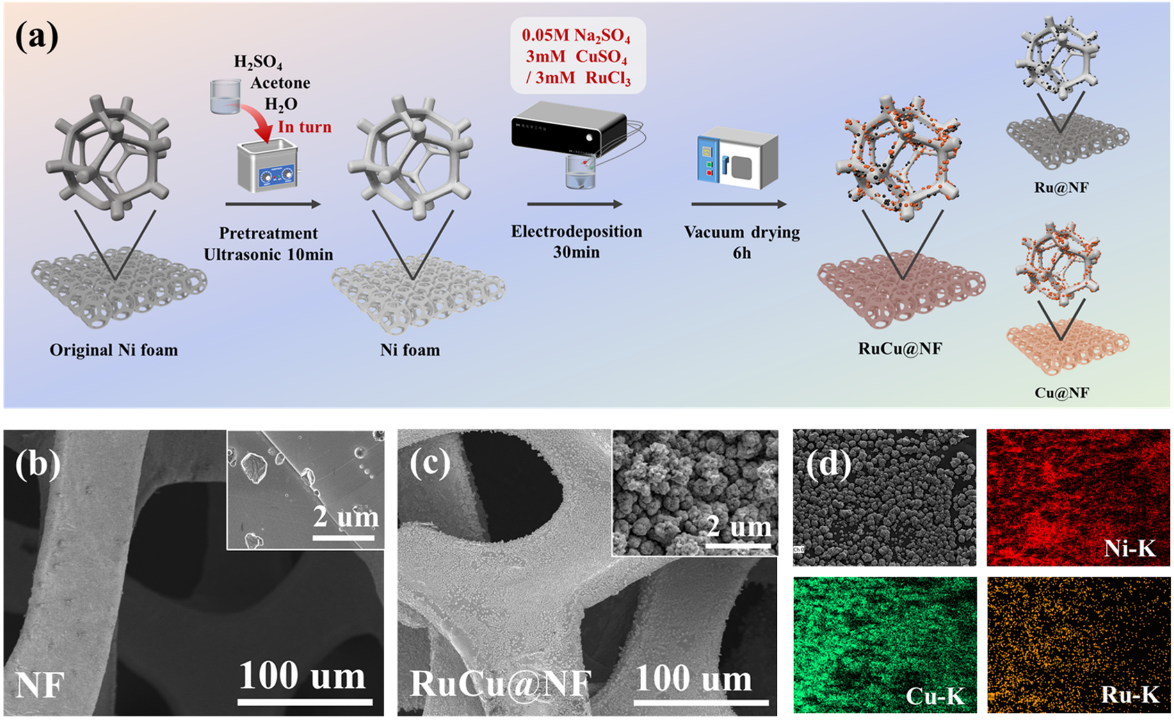

Figure 1. (a) Schematic illustration for the coelectrodeposition of RuCu@NF. SEM images of (b) NF and (c) RuCu@NF. Inset: the enlarged images. (d) EDX mapping results of RuCu@NF.

the most active single transition metal, with NH_3 as its primary product.[22−29] The high occupancy of Cu's *d* orbital energy level, comparable to the Lowest Unoccupied Molecular Orbital (LUMO) π^* of NO_3^-, facilitates nitrate adsorption and subsequent reduction, predominantly yielding NH_3.[5,30] However, the practical application of Cu is hindered by its susceptibility to deactivation due to the strong adsorption of intermediate N-containing species, leading to stability issues and reduced Faradaic efficiency.[29] Efforts to address this challenge have focused on modifying Cu nanostructures and developing heterogeneous structures, yet achieving 100% NH_3 selectivity remains elusive, accompanied by low Faraday efficiency. Moreover, the extensive use of metals in catalyst preparation translates to elevated costs. Alloying strategies have shown great potential in overcoming these challenges by combining two or more metals to leverage the synergistic effects of alloy components.[31] The introduction of another metal atom can enhance catalyst activity by promoting heteroatom doping at the atomic interface.[19] Alloy catalysts, particularly those incorporating noble metals such as Ru, Pt, Pd, and Au, have shown promise in enhancing NH_3 selectivity by virtue of their remarkable adsorption capabilities.[8,20,31−33] In alloy systems, the interaction between different metal atoms can lead to modified electronic structures, including changes in d-band center and charge distribution, which can fine-tune the adsorption strength of reaction intermediates and reduce undesired side reactions.[20,33] However, their tendency to excessively adsorb hydrogen often exacerbates competition with the hydrogen evolution reaction (HER), diminishing the Faraday efficiency of NH_3 production.[7,14,29] The high metal content further complicates the economic feasibility of these catalysts. Combining the structural advantages of the porous framework with the synergistic effect of bimetallicity has been proven to significantly enhance the catalytic activity. Ni foam is widely used as a substrate material in electrocatalytic reactions. Its unique porous structure not only increases the Electrochemical Surface Area (ECSA), but also enhances stability through heterostructures with metals.[34,35] Additionally, its self-activation properties allow it to form nickel hydroxide during electrocatalytic processes, which promotes ammonia selectivity.[36]

In the context of nitrate reduction, anodic reactions have traditionally been overlooked with the oxygen evolution reaction (OER) dominating the anode processes. However, replacing this sluggish OER with thermodynamically more favorable reactions holds significant promise.[37] Concurrently enhancing NH_3 production while generating high-value chemicals with exceptional selectivity poses a formidable challenge. Among anodic reactions, alcohol oxidation reactions (AORs) are particularly appealing due to their well-defined product spectra and pathways.[38,39] Recently, several studies have successfully coupled hydrogen production with the oxidation of benzyl alcohol to benzaldehyde, promoting both hydrogen generation and the synthesis of valuable chemicals.[40]

Herein, we present a novel approach that synergistically integrates cathodic NH_3 production with high yields via nitrate reduction with the anodic oxidation of benzyl alcohol to benzaldehyde. To this end, we employed a simple, one-step electrodeposition technique to incorporate small amounts of Ru into a copper-based Ni foam, yielding RuCu@NF. This technique facilitates the formation of alloys with variable compositions, harnessing the diverse ion transfer rates during preparation. Electrodeposition is widely employed in industrial catalyst synthesis owing to its simplicity and stability.[41] By fine-tuning the ion concentrations in the deposition solution, we effectively modulated the catalyst's properties, particularly the adsorption characteristics of active H* species, as substantiated by theoretical calculations. Our experimental findings demonstrate that the synthesized RuCu@NF catalyst achieves remarkable nearly 100% selectivity for NH_3. Furthermore,

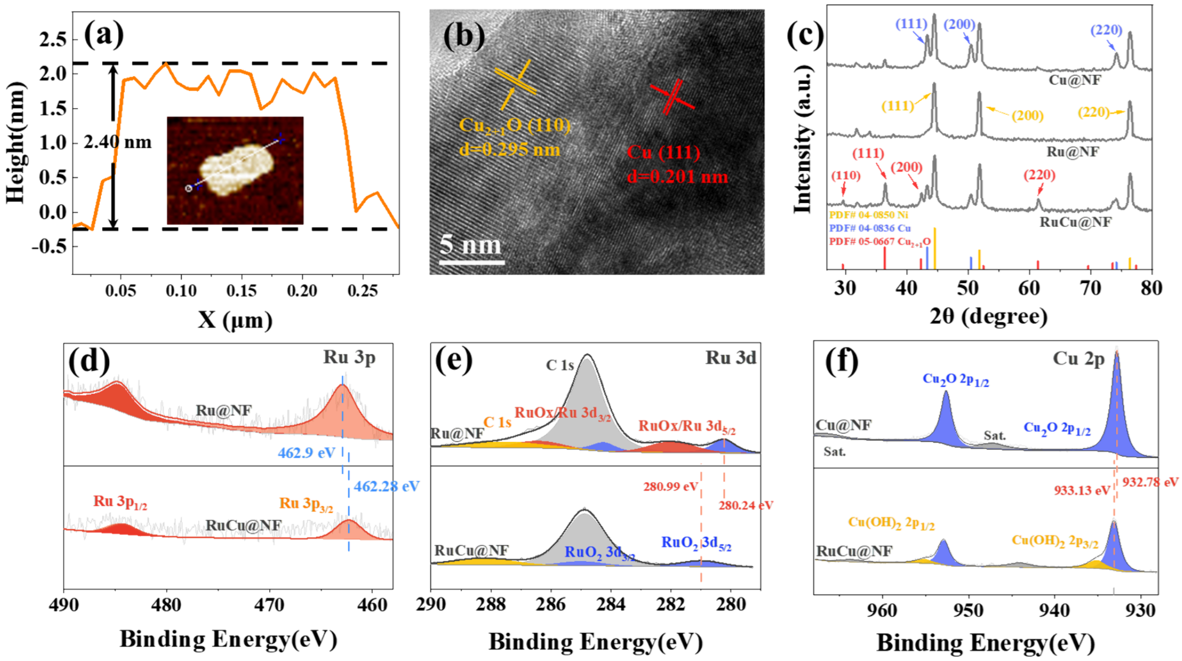

Figure 2. AFM images (a) and TEM images (b) of RuCu@NF with corresponding height curves. XRD patterns of RuCu@NF, Ru@NF and Cu@NF (c). XPS spectra: (d) Ru 3p spectra, (e) Ru 3d spectra, and (f) Cu 2p spectra of RuCu@NF, Ru@NF and Cu@NF.

the catalyst exhibited robust structural stability with only minimal activity loss after 10 consecutive cycles of nitrate reduction. We also devised a coupled system employing a split cell configuration that enabled the production of benzaldehyde through the concurrent nitrate reduction and oxidation of benzyl alcohol (BAO). This system not only significantly accelerated the nitrate reduction rate (approximately 1.7-fold increase in the rate constant to k = 0.04397 min^{-1}) but also achieved a high benzaldehyde conversion rate of 90%. This innovative approach not only avoids the inefficiencies associated with the OER but also underscores the potential of coupling nitrate reduction with the synthesis of high-value chemicals.

2. EXPERIMENTAL SECTION

2.1. Electrode Preparation and Electrochemical NO_3^--N Reduction Experiments. Prior to preparation, a nickel foam (NF) substrate of dimensions underwent a meticulous cleaning procedure. The RuCu@NF was synthesized via a one-step potentiostatic electrodeposition technique,[42] as depicted schematically in Figure 1a. A standard three-electrode system was assembled, with the NF substrate serving as the working electrode. The coelectrodeposition was carried out at a constant potential of -1.0 V vs Ag/AgCl for 30 min in an electrolyte solution containing $RuCl_3$, $CuSO_4$ and Na_2SO_4. The stability of the sedimentation process in this method is shown in Figure S1 and Table S1. Additionally, Cu-modified NF (referred to as Cu@NF) and Ru-modified NF (referred to as Ru@NF) electrodes were prepared using similar methods with varying concentrations of Ru and Cu salts in the deposition solution, as detailed in Table S2.

Electrochemical measurements for the NO_3RR were performed by using an electrochemical workstation (CHI 760E, CH Instruments, USA) in an undivided three-electrode configuration. The RuCu@NF electrode (20 nm × 30 nm), Pt sheet and Ag/AgCl were used as the working electrode, counter electrode and reference electrode, respectively. The solution (50 mL) contained $NaNO_3$ (50 ppm) provided source of NO_3^--N and Na_2SO_4 (0.05M) improved the solution electrical conductivity. Chronoamperometry (i-t) tests were conducted at −1.6 V vs Ag/AgCl under stirring (stirring rate: 400 rpm) for 2 h. To investigate the NO_3RR activity, 1 mL solution were taken out for the detection of NO_3^--N and NO_2^--N with ion chromatographic (IC, Thermo, ICS-1100) at 20 min intervals. Meanwhile, the concentration of NH_4^+-N was quantified with an ultraviolet−visible (UV−vis, UV-1800, Shimadzu, Japan) spectrophotometer. The remaining characterization is detailed in SI.

Density functional theory (DFT) calculations were performed using the VASP5.4.1 software package.[43−45] The generalized gradient approximation functional Perdew−Burke−Ernzerhof (PBE) was used for the exchange correlation functional, with the projected augmented wave (PAW) pseudopotential basis set and a cutoff energy of 400 eV.[46,47] The van der Waals interactions were considered using the DFT-D3 empirical correction.[48] The electronic energy was considered self-consistent when the energy change was smaller than 10−6 eV. A geometry optimization was considered convergent when the energy change was smaller than 0.01 eV Å−1. Thermodynamic Gibbs free energy corrections and density of states (DOS) analysis were carried out with the aid of the VASPKIT 1.2.1 tool package. The Brillouin zone integral uses the surface structures of 3 × 3 × 1 Monkhorst−Pack K-point sampling for structure. The Gibbs free energy of the reaction intermediates was calculated using the computational hydrogen electrode model, as shown below:

$$G = E_{DFT} + ZPE - Ts$$

Where E is the energy obtained from DFT calculations, ZPE is the zero-point energy of the material, S is the entropy of the adsorbate, and T is the thermodynamic temperature (298.15K).

2.2. Coupled System. The coupled experiments were performed in a H-type electrolytic cell utilizing a three-electrode system separated by a pretreated proton-exchange membrane (Nafion 117). The cathode compartment contained a solution of $NaNO_3$ (50 ppm) and Na_2SO_4 (0.05 M), while the anode compartments held various concentrations of benzyl alcohol. Both compartments had a volume of 30 mL. The electrochemical reaction was meticulously monitored by high-performance liquid chromatography (HPLC), as detailed in SI.

3. RESULTS AND DISCUSSION

3.1. Structural Characterization of Electrodes. The coelectrodeposition preparation process for fabricating RuCu@NF cathode is elucidated in Figure 1a, and its physical depiction is shown in Figure S2. The detailed characterization

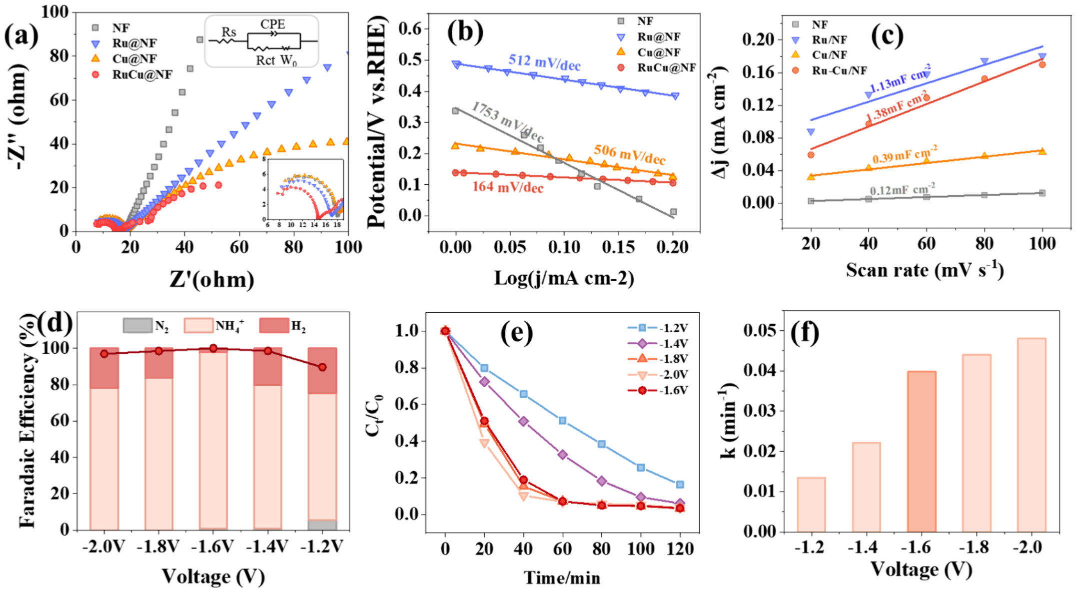

Figure 3. EIS nyquist plots (a) with an equivalent circuit model (inset), Tafel plots (b) and linear fitting of capacitive currents (c) of NF, Cu@NF, Ru@NF and RuCu@NF. Reaction conditions: 0.05 M Na_2SO_4 electrolyte at −1.6 V (vs Ag/AgCl); NO_3^- conversion and faradic efficiency (d), decay kinetics (e) and kinetic linear fitting (f) for NO_3^--N removal over different voltages. Reaction conditions: 50 ppm of NO_3^--N in 0.05 M Na_2SO_4 electrolyte.

results are shown in Figures 1 and 2. The scanning electron microscopy (SEM) images demonstrate that the surface of RuCu@NF, as well as Ru@NF and Cu@NF (Figure S3), exhibits a significantly roughened texture compared to the smooth Ni foam. This indicates the successful growth and uniform distribution of Ru and Cu nanoparticles on the Ni foam surface (Figure 1d). Notably, the macroporous framework of the Ni foam is retained. Furthermore, the atomic force microscopy (AFM) images depict a flake structure with an average thickness of 2.4 nm (Figure 2a). Transmission electron microscopy (TEM) image in Figure 2b highlights the polycrystalline nature of the RuCu@NF cathode, consisting of numerous ordered nanograins with distinct orientations. Two fringes corresponding to different lattice planes are observed, namely, the $Cu_{2+1}O$ (110) and Cu (111), with apparent distortion at the two-phase interface. These phases are confirmed by X-ray diffraction (XRD) characterization, as shown in Figure 2c. These results confirm that the primary composition of RuCu@NF comprises Cu and $Cu_{2+1}O$. Additionally, the absence of a significant Ru diffraction peak may be attributed to its small amount and amorphous form.[49] The amorphous and heterostructured nature may enhance NO_3RR reactivity by exposing more active sites. Inductively coupled plasma (ICP) analysis in Table. S3 reveals that the Ru content is minimal, accounting for only 1/9 of the Cu content. Moreover, electrodeposition leads to a marked improvement in the wettability of the Ni foam, with the contact angle decreasing from 121° to 62° (Figure S4).

To gain further insight into the surface composition and valence states, X-ray photoelectron spectroscopy (XPS) was employed. Full survey spectra in Figure S5 confirm the presence of Cu, Ru, Ni, and O elements. In the Ru 3p XPS spectra (Figure 2d), the peaks at 462.9 and 462.28 eV correspond to Ru 3p3/2. Notably, RuCu@NF exhibits lower binding energies in the Ru 3p peaks compared with Ru@NF, indicating effective electron transfer at the heterogeneous interface. C 1s spectra partially overlap with Ru 3d peaks, as shown in Figure 2e. Peaks at 280.24 and 280.99 eV are attributed to RuO_2, while the peak at 281.98 eV corresponds to RuO_x/Ru.[50] The presence of oxides results from sample exposure to air before testing. Cu 2p XPS peaks of RuCu@NF positively shift from 932.78 to 933.13 eV,[51,52] while Ru 3p orbital peaks negatively shift by 0.62 eV (Figure 2f). These shifts indicate that Cu doping can modulate the electronic structure of Ru, potentially influencing the adsorption behavior of reaction intermediates, thereby contributing to the enhanced performance of the RuCu@NF catalyst.

3.2. Optimized Catalytic Performance of Electrochemical Reduction.

The electrochemical impedance spectroscopy (EIS) analysis was employed to evaluate the charge transfer resistances, thereby gaining insights into the reaction kinetics and interface properties.[53] The descending order of arc size (NF > Cu@NF > Ru@NF> RuCu@NF) in Figure 3a suggested that RuCu@NF has the smallest arc radius, which verified this electrode had lowest charge transfer resistance. In Figure 3b, RuCu@NF exhibits a smaller Tafel slope (164 mV/dec) than the other three catalysts, corresponding to a faster kinetic reaction.[54,55] As shown in Figures 3c and S6, the electrochemically active surface area (ECSA) values of RuCu@NF (1.38 mF cm^{-2}) is higher than others, suggesting that Ru and Cu codoping increases the ECSA values and thus improves reactant dynamic reactant sites for NO_3RR. These electrochemical test results indicated that RuCu@NF has a lower charge transfer barrier than bared Ni foam or single atom doped.

Various electrolyte voltages were applied to optimize the NO_3RR performance regarding Faradaic efficiency, selectivity, and reduction rate. As illustrated in Figure 3d, Faradaic efficiencies follow a volcano-shaped trend from −2.0 V to −1.2 V, with NH_4^+-N reaching a maximum of 96.8% at −1.6 V. Notably, negligible NO_2^- byproducts were observed within a wide applied potential window. Conversely, at other potentials, the Faradaic efficiency decreased due to the dominance of the HER. Importantly, nitrogen formation was observed at

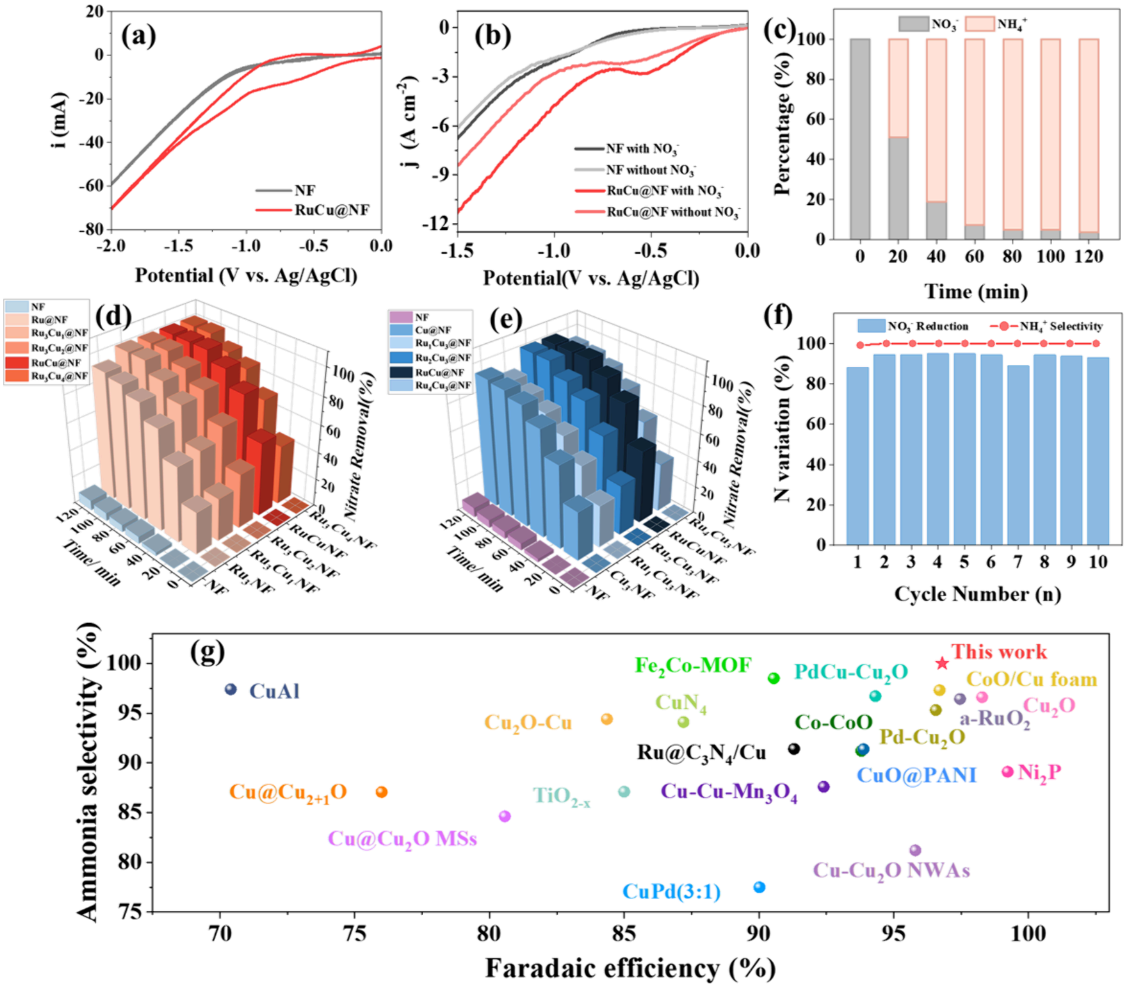

Figure 4. (a) LSV curves of NF and RuCu@NF in 0.05 M Na_2SO_4 solution at 10 mV s^{-1}. (b) CV curves of NF and RuCu@NF in 0.05 M Na_2SO_4 electrolyte in the absence and presence of 50 ppm of NO_3^- at 10 mV s^{-1}. (c) NO_3^- conversion process on RuCu@NF electrode. Physical drawings of catalysts of different atoms ratio. NO_3^--N removal process over different atom ratios (Ru_3Cu_y@NF (d) and Ru_xCu_3@NF (e)). (f) Recycling test of electrochemical reduction for 10 times. (g) FE values and NH_3 selectivity of RuCu@NF compared with other recently reported catalysts. Reaction conditions: 50 ppm of NO_3^--N in 0.05 M Na_2SO_4 electrolyte at −1.6 V (vs Ag/AgCl).

potentials as low as −1.2 V. Figure 3e and f reveals that the NO_3^--N removal rate gradually increases from 0.0135 min^{-1} to 0.0398 min^{-1} as the potential shifts from −1.2 V to −1.6 V. This increase is likely attributed to enhanced electron availability or atomic H* at more negative potentials. However, as potentials continue to rise, the removal rate stabilizes, suggesting that the increase in rate may not offset the decrease in energy utilization caused by higher voltages. Additionally, excess atomic H* tends to recombine into hydrogen gas, which can hinder the reaction by blocking active sites and impeding the adsorption of nitrate and intermediates. Consequently, −1.6 V emerges as the optimal potential for this system.

The electrochemical performance of RuCu@NF and bare NF, as well as Cu@NF and Ru@NF, were first assessed using cyclic voltammetry (CV) in a 0.05 M Na_2SO_4 solution, as shown in Figures 4a and S7. The CV curves reveal distinct hydrogen adsorption and desorption peaks within the potential range of −2.0 to 0 V, indicating the electrochemical activity of the prepared catalysts. Notably, the larger peak areas for RuCu@NF suggest a higher ECSA compared to those of the other three catalysts, which is consistent with the ECSA measurement presented in Figure 3c. To evaluate the NO_3RR performance, Linear Sweep Voltammetry (LSV) was conducted in a solution containing 50 ppm of NO_3^- and 0.05 M Na_2SO_4, as illustrated in Figures 4b and S8. Upon the addition of NO_3^-, both RuCu@NF and NF exhibited an increase in reduction current, confirming their electrocatalytic activity toward NO_3RR. Among them, RuCu@NF showed a superior initial reduction potential and higher reduction currents, suggesting its enhanced electrochemical activity. This improvement can be attributed to the abundant active sites and synergistic effects between Ru and Cu in the RuCu@NF catalyst. The reduction current of NF gradually increases as the potential becomes more negative, in both the presence and absence of NO_3^-, indicating HER activity. At the same time, the two curves show little difference, suggesting strong interference from HER, with almost no nitrate reduction activity. This significantly reduces the FE and selectivity for ammonia conversion, particularly at more negative potentials, where positively charged protons are more favorable for reduction than negatively charged nitrates due to electrostatic interactions.[56] In stark contrast, on the RuCu@NF, nitrate reduction is more favorable with the addition of nitrate significantly enhancing the current density. As shown in Figure S8, the curve of Ru@NF shows less difference in the presence or absence of NO_3^- compared to Cu@NF, further confirming

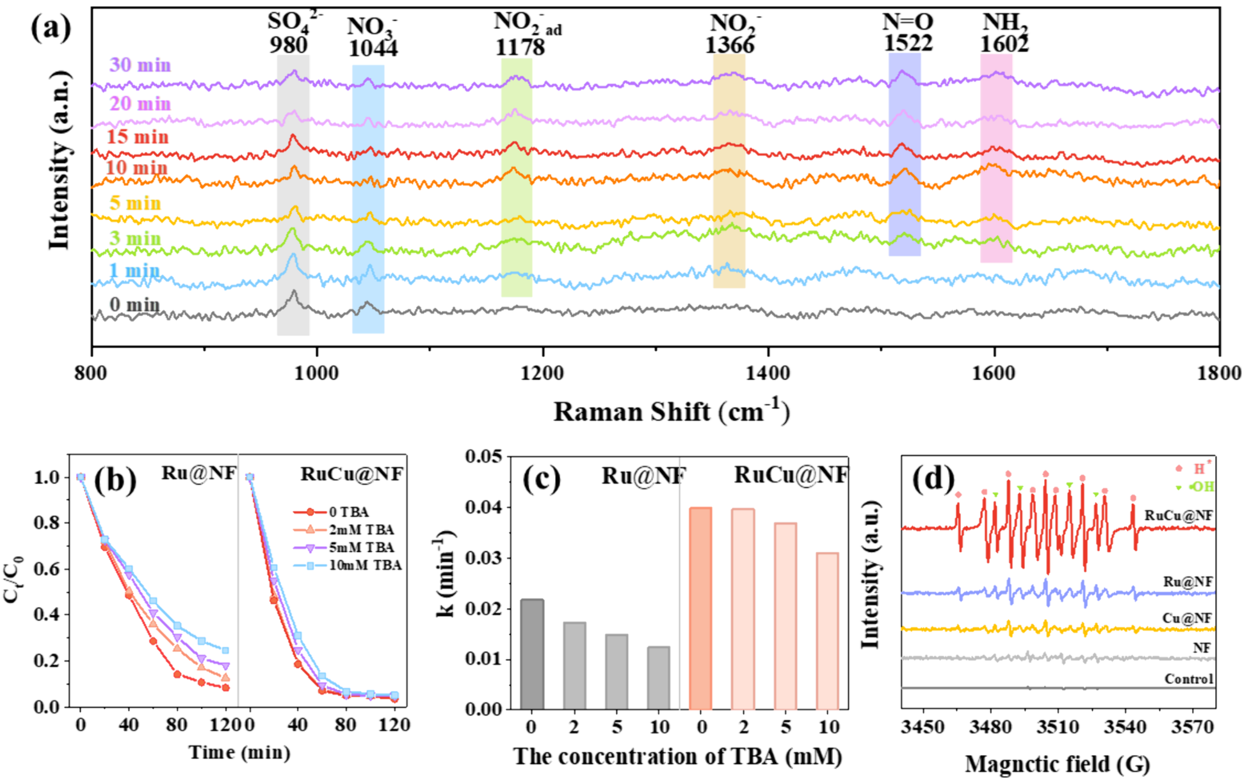

Figure 5. (a) In situ Raman spectra of NO_3RR with the RuCu@NF electrode in 0.05 M Na_2SO_4 (with 0.1 M NO_3^--N). (b) Concentration removal of NO_3^--N at the Ru_3@NF and Ru_3Cu_3@NF cathode with various TBA concentrations. (c) Reaction rate constant of the kinetic fit for the Ru_3@NF and Ru_3Cu_3@NF cathode with various TBA concentrations. (d) DMPO spin-trapping EPR spectra with different electrode. Reaction conditions: 50 ppm of NO_3^--N with 0.05 M Na_2SO_4 electrolyte in cathode cell while 0, 2, 5, and 10 mg/L BA with 0.05 M Na_2SO_4 electrolyte in anode cell at −1.6 V (vs Ag/AgCl).

that Ru mainly provides adsorbed hydrogen (which facilitates the HER reaction), while Cu primarily promotes nitrate reduction (making nitrate reduction more favorable). The effective regulation of both elements ultimately results in a 100% ammonia selectivity. Further investigation of the nitrate reduction process at the optimal potential of −1.6 V revealed that the RuCu@NF cathode achieved a remarkable 96.5% removal of NO_3^--N within 120 min in a single cell, with nearly 100% selectivity toward ammonia and no observable byproducts (Figure 4c). This superior selectivity and removal efficiency underscore the exceptional catalytic performance of RuCu@NF.

The influence of different ratios of the Ru and Cu elements on the nitrate reduction performance was systematically evaluated. As expected, bare Ni foam displayed the lowest activity due to its limited active sites. When the Cu^{2+} concentration was held constant at 3 mM and the Ru^{3+} ratio varied in the electrodeposition electrolyte, a volcano-shaped trend in reduction ability was observed (Figure 4d). This trend can be attributed to the optimal balance between active site density and c dispersion. An increase in Cu^{2+} concentration resulted in more nanoparticles and active sites, but excessive Cu^{2+} led to nanoparticle clustering, hindering nitrate adsorption and the reaction. Conversely, when the Cu^{2+} concentration was fixed and the Ru^{3+} ratio was varied, a different trend emerged (Figure 4e). The descending order of nitrate reduction ability was RuCu@NF > Ru_2Cu_3@NF > Cu_3@NF > Ru_4Cu_3@NF > Ru_1Cu_3@NF > NF. This variation suggests that the distinct roles of Ru and Cu in the catalytic process contribute to the observed performance differences, which will be discussed in detail in subsequent sections. The long-term stability of the RuCu@NF catalyst is crucial for practical applications. As shown in Figure 4f, the 10-cycle NO_3^--N electroreduction experiments exhibited acceptable activity degradation, indicating robust structural stability. Additionally, the leaching of Cu ions (7.6048 μg L^{-1}, Table S4) was significantly lower than the regulatory limit specified in GB/T 25467−2010 in China (0.2 mg L^{-1}), and Ru loss was also within acceptable limits. Notably, except for the first cycle, NH_4^+ selectivity remained stable at 100%, further validating the catalyst's exceptional performance. In summary, the RuCu@NF catalyst exhibits one of the best performances reported to date for the NO_3RR to ammonia, as evidenced by its high removal efficiency, selectivity, and long-term stability (Figure 4g and Table S5). These results demonstrate the effectiveness of the proposed one-step electrodeposition method in preparing high-performance electrocatalysts for nitrate reduction.

3.3. Electrocatalytic Mechanism of RuCu@NF on Nitrate Reduction. To gain deeper insights into the nitrate reduction mechanism leading to ammonia production at the RuCu@NF cathode under −1.6 V, we conducted in situ electrochemical Raman spectroscopy measurements. (The schematic diagram and actual device image are shown in Figure S9.) As depicted in Figure 5a, and the characteristic Raman bands centered at 1044 cm^{-1} were attributed to the vibration modes of aqueous NO_3^-. Notably, during the reaction, the intensity of this band diminished, reflecting the gradual depletion of nitrate in the solution. Concurrently, we observed an enhanced peak intensities associated with the

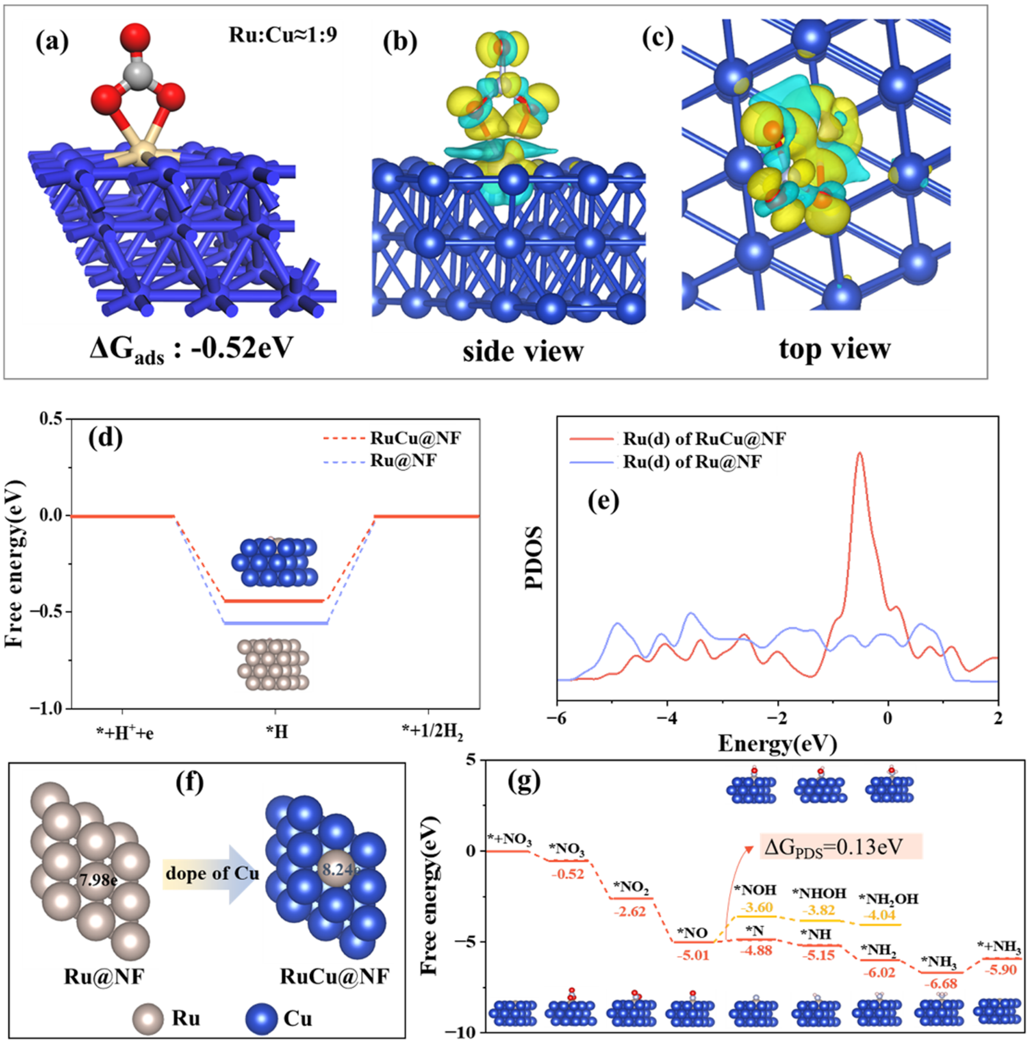

Figure 6. (a) NO_3^- adsorption on RuCu@NF. (b) Side view of differential charge densities of the NO_3^- adsorption on RuCu@NF. (c) Top view of differential charge densities of the NO_3^- adsorption on RuCu@NF. (d) Free energy diagrams of the HER process on RuCu@NF and Ru@NF. (e) PDOS of Ru(d) for RuCu@NF and Ru@NF. (f) Bader charge of the central Ru atom of Ru@NF and RuCu@NF. (g) Free energy diagrams of $NO_3 \rightarrow NH_3$ on RuCu@NF. Dark blue, silver, red, light blue, and gray balls represent Cu, Ru, O, N, and H atoms, respectively.

adsorbed $NO_2^-{}_{ad}$ (1178 cm^{-1}) and NO_2^- (1366 cm^{-1}) in the contour plots, strongly suggesting the accumulation of intermediate species during the reduction process. While the presence of nitrite was spectroscopically discernible, its concentration fell below the detection limit of ion chromatography, rendering its contribution to the overall reaction negligible. Critically, The emergence of Raman peaks at 1602 cm^{-1} during the reaction progression could be attributed to the stretching vibration of H—N—H bonds, serving as direct evidence for the effective reduction of nitrate to ammonia on the RuCu@NF cathode surface. Furthermore, these H—N—H bond-related peaks appeared earlier than those on bare NF electrodes (Figure S10), indicating the superior nitrate reduction capability of RuCu@NF composite. This observation highlights the efficacy of our RuCu@NF catalyst in driving the nitrate reduction reaction toward ammonia production.

The electrochemical NO_3RR process is well established as predominantly relying on two mechanisms: direct electron transfer and indirect reduction mediated by atomic hydrogen (H*). Previous studies have shown that direct electron transfer is favored on nonprecious metal cathodes (e.g., Cu) due to their strong absorption of NO_3^-. Conversely, noble metal cathodes (e.g., Ru) mediate the NO_3RR through atomic H*. Cu is renowned for adsorbing NO_3^- effectively, which is then reduced to the NO_2^- (ad) at the active site, marking the rate limiting step in the NO_3RR. Subsequently, NO_2^- transforms into other N-containing intermediates, ultimately yielding NH_3.

In the indirect pathway, H* is generated via electron consumption according to the Volmer Formula, accompanied by H^+ consumption and a pH increase in the solution. Generally, the *tert*-butyl alcohol (TBA) employed to scavenge H*, forming inert 2-methyl-2-propanol radicals that do not interfere with NO_3RR. This allows us to verify the role of atomic H* in the catalyst.[57] As illustrated in Figure 5b and c, the NO_3^- removal efficiency of the Ru_3@NF cathode decreased significantly from 91.7% to 75.3% as the TBA concentration increased from 0 to 10 mM, indicating reliance on the H*-mediated indirect pathway. In contrast, the pronounced decay kinetics observed for the Ru_3@NF electrode exhibited more significant variations in response to the TBA concentration than those for the Ru_3Cu_3@NF electrode. Over a two h interval, the NO_3^- removal efficiency for the Ru_3Cu_3@NF cathode remained relatively stable.

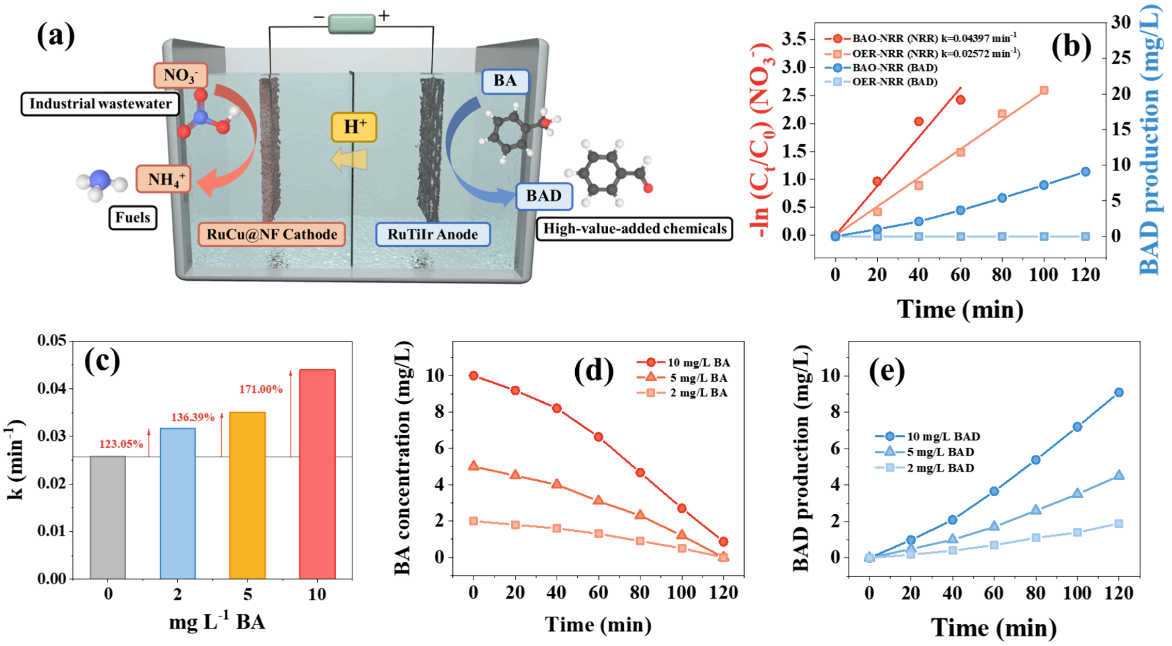

Figure 7. (a) Schematic illustration for the coupled system. (b) Kinetic linear fitting for NO_3^--N removal and BAD production of OER coupled NO_3RR and BA oxidation coupled NO_3RR under the potential of −1.6 V. (c) Decay kinetics for NO_3^--N removal over different BA initial concentrations. (d) Process of BA oxidation during the reaction. (e) Process of BAD production during the reaction. Reaction conditions: 50 ppm of NO_3^--N with 0.05 M Na_2SO_4 electrolyte in cathode cell while 0, 2, 5, and 10 mg/L BA with 0.05 M Na_2SO_4 electrolyte in anode cell at −1.6 V (vs Ag/AgCl).

Although the kinetics constant declined from 0.0398 min^{-1} to 0.0309 min^{-1}, this decrease had negligible implications for the overall NO_3RR (Figure 5c). Therefore, it is reasonable to speculate that the NO_3RR on Ru_3@NF follows the theory of an indirect pathway mediated by absorbed H* during the electrochemical NO_3RR process. Besides, the NO_3RR reaction mechanism on Ru_3Cu_3@NF is more intricate as it exhibits superior reactivity with less pronounced changes in response. However, it is certain that the presence of H* in the reaction solution must be much greater when doping with Ru alone. Furthermore, DMPO (5,5-dimethyl-1-pyrroline N-oxide) spin-trapping EPR spectra were employed to identify the presence of H*, corroborating the TBA test in the NO_3RR process. As shown in Figure 5d, all electrodes exhibited characteristic peaks of DMPO-H and the hydroxyl radical, respectively, with nothing observed in the control experiment. The presence of hydroxyl radicals likely results from the oxygen reduction reaction in an open cell, as the influence of anode free radicals is eliminated in a divided cell. Notably, the peaks associated with Ru_3Cu_3@NF were higher than those for Ru_3@NF and Cu_3@NF individually or even when combined. This further validates the results of previous free radical scavenging experiments. Additionally, Ru was found to generate more H* than Cu, emphasizing its crucial role in H* production. Overall, these findings underscore the intricate yet efficient H*-mediated nitrate reduction pathway on the RuCu@NF electrode.

To gain deeper insights into the atomic and electronic mechanisms underpinning our observations, we performed comprehensive density functional theory (DFT) calculations. Our initial focus was on elucidating the intrinsic electronic structural changes of Ru@NF before and after Cu doping, particularly assessing their impact on H* adsorption capabilities. Figure 6a illustrates the schematic structure postadsorption, with an adsorption free energy of −0.52 eV, indicating the spontaneous nature of this process. Figure 6b further highlights the difference in charge density before and after NO_3^- adsorption, where the yellow and cyan planes represent charge accumulation and loss, respectively. Notably, the metal doping enhances surface charge heterogeneity, facilitating pronounced charge transfer between the adsorbed molecules. Expanding our analysis, we investigated the effects of Cu doping on the H* adsorption capability of Ru@NF. As shown in Figure 6d, pure Ru@NF exhibits a higher H* adsorption capacity in comparison to Cu-doped Ru@NF (RuCu@NF). To gain a nuanced understanding, we delved into the Partial Density of States (PDOS) of the central Ru atoms' d orbitals for both cases (Figure 6e). Out findings reveal that Ru atoms surrounded by Cu display a higher electron distribution near the Fermi level. Additionally, Bader charge analysis (Figure 6f) revealed that Cu doping leads to an increase in charge on the Ru atoms, reducing their electron-accepting capability of Ru and subsequently diminishing their Lewis acidity and H* adsorption capacity. At first glance, the DFT results indicating greater H* adsorption capability for pure Ru@NF than RuCu@NF may seem at odds with our radical scavenging and EPR measurements. However, this apparent contradiction can be rationalized as follows: The hydrogen generated by Ru alone is more prone to evolving into hydrogen gas (HER) rather than being trapped by TBA or DMPO. In essence, the HER is so rapid that it hampers the capture of these free H* species. Conversely, the incorporation of Cu with Ru acts as an "anchor" for H*, inhibiting the HER and ensuring the availability of H* for subsequent ammonia production. Furthermore, the hydrogenation process from *N to *+NH_3, as depicted in Figure 6g, is spontaneous, unlike the energy-intensive HER process outlined in Figure 6d. These findings provide compelling evidence for the synergistic effect between Ru and Cu in enhancing the efficiency and selectivity of reduction of nitrate to NH_3.

The intricate interplay between the doping ratios of Ru and Cu significantly impacts the nitrate reduction rates during the 2 h reaction, as evidenced in Figure 4d. When the Ru^{3+} concentration is held constant and the Cu^{2+} proportion is varied, the electrode's reduction capacity first surges and then tapers off. This phenomenon can be attributed to Cu's capability to "anchor" the atomic H* generated by Ru on the Ni foam surface, thereby facilitating nitrate reduction and ammonia production. Nevertheless, excessive Cu^{2+} leads to H* accumulation, shifting the reaction toward HER instead of ammonia formation. Shifting focus to Figure 4e, where the Cu^{2+} concentration is fixed at 3 mM while Ru^{3+} concentration varies in the electrodeposition solution, reveals a more intricate scenario. In the absence of Ru^{3+} (Cu_3@NF), the nitrate reduction rate surpasses that of Ru_1Cu_3@NF, likely due to Ru occupying active Cu sites on the Ni foam. Furthermore, as the Ru^{3+} proportion increases, so does the H* production. Notably, the contrasting trends in nitrate reduction rate and ammonia selectivity (Figure S11b) suggest that Cu utilized some of the active site of $NO_3^-{}_{ad}$ to "anchor" H* from Ru. In other words, Cu compromises part of its adsorption and reduction ability to enhance the NH_3 selectivity. This observation reinforces our previously proposed catalytic mechanism.

To delve deeper into the reaction pathway and catalytic mechanism of the RuCu@NF, we constructed adsorption models for various reactants and intermediates ($*NO_3$, $*NO_2$, *NO, *N(*NOH), *NH(*NHOH), $*NH_2(*NH_2OH)$, and $*NH_3$) involved in the nitrate reduction to NH_3 process, as shown in Figure 6g. Among the two plausible pathways, *NO preferentially follows the O losing route to form *N, constituting the rate-limiting step with a Gibbs free energy change of 0.13 eV. Consequently, the electrochemical nitrate reduction to NH_3 could be summarized as follows: (1) NO_3^--adsorption and activation into free radical * NO_3^-; (2) $*NO_3$ undergoes deoxygenation to generate *NO; (3) *NO loses O to form *N; (4) sequential hydrogenation steps to form * NH_3 formation through proton-coupled electron transfer; and (5) NH_3 desorption. These findings align with experimental data, elucidating the exceptional NO_3RR activity and high ammonia selectivity on the RuCu@NF cathode, underscoring the crucial role of atomic H* in the NO_3RR.

3.4. Optimization of Coupled Anodic Reaction with Nitrate Reduction. In optimizing the coupling of benzyl alcohol oxidation (BAO) with nitrate reduction, we conducted a thorough assessment of the NO_3RR performance of the RuCu@NF within a three-electrode split-cell configuration, as shown in Figure.S12. The substitution of the OER with BAO at the anode, coupled with the enhanced cathodic activity on the RuCu@NF, significantly bolstered the NO_3RR efficiency. This innovative coupled system delivered remarkable results, achieving equivalent NO_3^--N removal in a substantially shortened time frame compared to NO_3RR coupled with OER. As shown in Figure 7a, at an initial BA concentration of 10 mg/L and a constant cell voltage of −1.60 V, the NO_3RR-BAO system demonstrated a swift removal rate of 0.04397 min^{-1}, outperforming the NO_3RR-OER system by a substantial margin of approximately 1.7-fold (0.02572 min^{-1}). Notably, the NO_3RR-BAO system accomplished complete BAO with consistent 100% conversion, yielding benzaldehyde with a high selectivity exceeding 90%. Conversely, the NO_3RR-OER system failed to generate any high-value-added chemicals. Furthermore, as illustrated in Figure 7c, upon varying the initial concentration of BA, we observed a pronounced increase in the nitrate reduction rate, while maintaining a consistently high selectivity toward BAO over 90% (Figure 7d and e). These findings underscore the exceptional capabilities of the RuCu@NF cathode, when coupled with a suitable anode material such as RuTiIr, to efficiently remove nitrate while concurrently producing both ammonia and high-value-added chemicals, holding great potential for applications in wastewater treatment and sustainable chemistry.

4. CONCLUSION

This study demonstrates that RuCu@NF nitrate reduction catalysts prepared by simple electrodeposition alone achieve a remarkable 96.5% removal of NO_3^--N within 120 min, with nearly 100% selectivity toward ammonia, and no observable byproducts were generated by adjusting the proportion of deposited metals. Both DFT calculations and experimental validations affirm that the introduction of Cu exerts an "anchoring" effect on H*, which is generated subsequent to that of Ru. Furthermore, the electrochemical coupling system employing this catalyst exhibits a substantially accelerated nitrate reduction rate, with the rate constant increasing by approximately 1.7-fold (from 0.02572 to 0.04397 min^{-1}) under identical conditions. Concurrent with this, benzyl alcohol can be oxidized at the anode, achieving 90% selectivity for benzaldehyde. The electrodeposition method used in this study is simple and convenient, making it highly suitable for practical industrial applications with a significant industrial value. Moreover, the synergistic electrocatalysis approach not only replaces the anodic oxygen evolution reaction, enhancing the cathodic reduction rate, but also offers new insights into the integration of nitrate reduction and the synthesis of high-value-added chemicals.

■ ASSOCIATED CONTENT

Supporting Information

The Supporting Information is available free of charge at https://pubs.acs.org/doi/10.1021/cbe.4c00124.

> Additional experimental details, materials, and methods, including photographs of experimental setup, calculation method, data of the electrodeposition process, contact angle picture, XPS survey spectrum, ECSA current densities pictures, in situ Raman spectra, tables of ICP test results, summary of the performance of the recent NO3RR catalysts (PDF)

■ AUTHOR INFORMATION

Corresponding Authors

Shaodong Zhou − *Key Laboratory of Biomass Chemical Engineering of Ministry of Education, College of Chemical and Biological Engineering, Zhejiang University, Hangzhou 310058, China; Institute of Zhejiang University-Quzhou, Quzhou 324000, China;* orcid.org/0000-0003-3048-4678; Email: szhou@zju.edu.cn

Bin Yang − *Key Laboratory of Biomass Chemical Engineering of Ministry of Education, College of Chemical and Biological Engineering, Zhejiang University, Hangzhou 310058, China; Institute of Zhejiang University-Quzhou, Quzhou 324000, China;* orcid.org/0000-0002-5136-9743; Email: keyangb@zju.edu.cn

Authors

Shuyi Shen − *Key Laboratory of Biomass Chemical Engineering of Ministry of Education, College of Chemical and Biological Engineering, Zhejiang University, Hangzhou 310058, China*

Shuyue Wang − *Key Laboratory of Biomass Chemical Engineering of Ministry of Education, College of Chemical and Biological Engineering, Zhejiang University, Hangzhou 310058, China; Institute of Zhejiang University-Quzhou, Quzhou 324000, China*

Bo Zhang − *Key Laboratory of Biomass Chemical Engineering of Ministry of Education, College of Chemical and Biological Engineering, Zhejiang University, Hangzhou 310058, China*

Xuesong Zhao − *Key Laboratory of Biomass Chemical Engineering of Ministry of Education, College of Chemical and Biological Engineering, Zhejiang University, Hangzhou 310058, China; Institute of Zhejiang University-Quzhou, Quzhou 324000, China;* orcid.org/0000-0002-2512-9826

Chen Sun − *Key Laboratory of Biomass Chemical Engineering of Ministry of Education, College of Chemical and Biological Engineering, Zhejiang University, Hangzhou 310058, China; Institute of Zhejiang University-Quzhou, Quzhou 324000, China*

Zhongjian Li − *Key Laboratory of Biomass Chemical Engineering of Ministry of Education, College of Chemical and Biological Engineering, Zhejiang University, Hangzhou 310058, China; Institute of Zhejiang University-Quzhou, Quzhou 324000, China;* orcid.org/0000-0002-3685-381X

Yang Hou − *Key Laboratory of Biomass Chemical Engineering of Ministry of Education, College of Chemical and Biological Engineering, Zhejiang University, Hangzhou 310058, China; Institute of Zhejiang University-Quzhou, Quzhou 324000, China;* orcid.org/0000-0001-9795-8503

Lecheng Lei − *Key Laboratory of Biomass Chemical Engineering of Ministry of Education, College of Chemical and Biological Engineering, Zhejiang University, Hangzhou 310058, China; Institute of Zhejiang University-Quzhou, Quzhou 324000, China*

Complete contact information is available at:
https://pubs.acs.org/10.1021/cbe.4c00124

Author Contributions

[§]S.S. and S.W. contributed equally to this work.

Notes

The authors declare no competing financial interest.

■ ACKNOWLEDGMENTS

This work was financially supported by the National Natural Science Foundation of China (22278366 and 22238008).

■ REFERENCES

(1) Xu, S.; Shi, Y.; Wen, Z.; Liu, X.; Zhu, Y.; Liu, G.; Gao, H.; Sun, L.; Li, F. Polystyrene Spheres-templated Mesoporous Carbonous Frameworks Implanted with Cobalt Nanoparticles for Highly Efficient Electrochemical Nitrate Reduction to Ammonia. *Appl. Catal., B* **2023**, *323*, 122192.

(2) Zhou, J.; Wen, M.; Huang, R.; Wu, Q.; Luo, Y.; Tian, Y.; Wei, G.; Fu, Y. Regulating Active Hydrogen Adsorbed on Grain Boundary Defects of Nano-nickel for Boosting Ammonia Electrosynthesis from Nitrate. *Energy Environ. Sci.* **2023**, *16*, 2611−2620.

(3) Wang, S.; Li, L.; Hui, K.; Dinh, D.; Lu, Z.; Zhang, Q.; Hui, K. Non-noble Single-atom Alloy for Electrocatalytic Nitrate Reduction Using Hierarchical High-throughput Screening. *Nano Energy* **2023**, *113*, 108543.

(4) Liu, M.; Miller, D.; Tarpeh, W. Reactive Separation of Ammonia from Wastewater Nitrate Via Molecular Electrocatalysis. *Environ. Sci. Technol. Lett.* **2023**, *10*, 458−463.

(5) Fu, Y.; Wang, S.; Wang, Y.; Wei, P.; Shao, J.; Liu, T.; Wang, G.; Bao, X. Enhancing Electrochemical Nitrate Reduction to Ammonia over Cu Nanosheets Via Facet Tandem Catalysis. *Angew. Chem., Int. Ed.* **2023**, *62*, No. e202303327.

(6) Liu, P.; Yan, J.; Huang, H.; Song, W. Cu/Co Bimetallic Conductive Mofs: Electronic Modulation for Enhanced Nitrate Reduction to Ammonia. *Chem. Eng. J.* **2023**, *466*, 143134.

(7) Zhang, Z.; Hong, Q.; Wang, X.; Huang, H.; Li, S.; Chen, Y. Au Nanowires Decorated Ultrathin Co_3O_4 Nanosheets toward Light-Enhanced Nitrate Electroreduction. *Small* **2023**, *19*, 2300530.

(8) Han, M.; Kani, K.; Na, J.; Kim, J.; Bando, Y.; Ahamad, T.; Alshehri, S.; Yamauchi, Y. Retrospect and Prospect: Nanoarchitectonics of Platinum-Group-Metal-Based Materials. *Adv. Funct. Mater.* **2023**, *33*, 2301831.

(9) Wang, Z.; Liu, S.; Wang, M.; Zhang, L.; Jiang, Y.; Qian, T.; Xiong, J.; Yang, C.; Yan, C. In Situ Construction of Metal-Organic Frameworks as Smart Channels for the Effective Electrocatalytic Reduction of Nitrate at Ultralow Concentrations to Ammonia. *ACS Catal.* **2023**, *13*, 9125−9135.

(10) Yu, Y.; Wang, C.; Yu, Y.; Wang, Y.; Zhang, B. Promoting Selective Electroreduction of Nitrates to Ammonia over Electron-deficient Co Modulated by Rectifying Schottky Contacts. *Sci. China Chem.* **2020**, *63*, 1469−1476.

(11) Yao, Q.; Chen, J.; Xiao, S.; Zhang, Y.; Zhou, X. Selective Electrocatalytic Reduction of Nitrate to Ammonia with Nickel Phosphide. *ACS Appl. Mater. Interfaces.* **2021**, *13*, 30458−30467.

(12) Liu, L.; Xiao, T.; Fu, H.; Chen, Z.; Qu, X.; Zheng, S. Construction and Identification of Highly Active Single-atom Fe_1-NC Catalytic Site for Electrocatalytic Nitrate Reduction. *Appl. Catal., B* **2023**, *323*, 122181.

(13) Lv, F.; Sun, M.; Hu, Y.; Xu, J.; Huang, W.; Han, N.; Huang, B.; Li, Y. Near-unity Electrochemical Conversion of Nitrate to Ammonia on Crystalline Nickel Porphyrin-based Covalent Organic Frameworks. *Energy Environ. Sci.* **2023**, *16*, 201−209.

(14) Lv, Y.; Ke, S.; Gu, Y.; Tian, B.; Tang, L.; Ran, P.; Zhao, Y.; Ma, J.; Zuo, J.; Ding, M. Highly Efficient Electrochemical Nitrate Reduction to Ammonia in Strong Acid Conditions with Fe_2M-trinuclear-cluster Metal-organic Frameworks. *Angew. Chem., Int. Ed.* **2023**, *62*, No. e202305246.

(15) Wang, H.; Man, S.; Wang, H.; Presser, V.; Yan, Q.; Zhang, Y. Grave-to-cradle Upcycling of Harmful Algal Biomass into Atomically Dispersed Iron Catalyst for Efficient Ammonia Electrosynthesis from Nitrate. *Appl. Catal., B* **2023**, *332*, 122778.

(16) Wang, J.; Cai, C.; Wang, Y.; Yang, X.; Wu, D.; Zhu, Y.; Li, M.; Gu, M.; Shao, M. Electrocatalytic Reduction of Nitrate to Ammonia on Low-cost Ultrathin CoO_x Nanosheets. *ACS Catal.* **2021**, *11*, 15135−15140.

(17) Zhao, T.; Li, X.; Hu, J.; Zhou, J.; Jia, X.; Hu, G. P-doped $FeCO_2O_4$ in-situ Decorated on Carbon Cloth as Robust Electrocatalysts for Reducing Nitrate and Nitrite to Ammonia. *J. Environ. Chem. Eng.* **2023**, *11*, 110122.

(18) Zhou, J.; Wen, M.; Huang, R.; Wu, Q.; Luo, Y.; Tian, Y.; Wei, G.; Fu, Y. Regulating Active Hydrogen Adsorbed on Grain Boundary Defects of Nano-nickel for Boosting Ammonia Electrosynthesis from Nitrate. *Energy Environ. Sci.* **2023**, *16*, 2611−2620.

(19) Wang, Z.; Liu, S.; Zhao, X.; Wang, M.; Zhang, L.; Qian, T.; Xiong, J.; Yang, C.; Yan, C. Interfacial Defect Engineering Triggered by Single Atom Doping for Highly Efficient Electrocatalytic Nitrate Reduction to Ammonia. *ACS Materials Letters* **2023**, *5*, 1018−1026.

(20) Zhou, Y.; Zhang, L.; Wang, M.; Zhu, Z.; Li, N.; Qian, T.; Yan, C.; Lu, J. Achieving near 100% Faradaic Efficiency of Electrocatalytic

Nitrate Reduction to Ammonia on Symmetry-Broken Medium-Entropy-Alloy Metallene. *ACS Catal.* **2024**, *14*, 7907−7916.

(21) Shen, S.; Wang, S.; Jia, Y.; Wu, B.; Tan, S.; Chen, Q.; Zhang, B.; Zhao, X.; Sun, C.; Zhou, S.; Li, Z.; Hou, Y.; Lei, L.; Yang, B. Tailoring Ni 3d Orbitals in Ni-Fe/Ni Foam Heterostructures for Enhanced H* Adsorption and Boosted Electrocatalytic Nitrate Reduction Performance. *Sep. Purif. Technol.* **2024**, *349*, 127867.

(22) Fu, W.; Du, Y.; Jing, J.; Fu, C.; Zhou, M. Highly Selective Nitrate Reduction to Ammonia on CoO/Cu Foam Via Constructing Interfacial Electric Field to Tune Adsorption of Reactants. *Appl. Catal., B* **2023**, *324*, 122201.

(23) Ren, T.; Ren, K.; Wang, M.; Liu, M.; Wang, Z.; Wang, H.; Li, X.; Wang, L.; Xu, Y. Concave-Convex Surface Oxide Layers over Copper Nanowires Boost Electrochemical Nitrate-to-Ammonia Conversion. *Chem. Eng. J.* **2021**, *426*, 130759.

(24) Jiang, M.; Zhu, Q.; Song, X.; Gu, Y.; Zhang, P.; Li, C.; Cui, J.; Ma, J.; Tie, Z.; Jin, Z. Batch-Scale Synthesis of Nanoparticle-Agminated Three-Dimensional Porous Cu@Cu_2O Microspheres for Highly Selective Electrocatalysis of Nitrate to Ammonia. *Environ. Sci. Technol.* **2022**, *56*, 10299−10307.

(25) Wang, C.; Ye, F.; Shen, J.; Xue, K.; Zhu, Y.; Li, C. In Situ Loading of Cu_2O Active Sites on Island-like Copper for Efficient Electrochemical Reduction of Nitrate to Ammonia. *ACS Appl. Mater. Interfaces.* **2022**, *14*, 6680−6688.

(26) Wang, Y.; Zhou, W.; Jia, R.; Yu, Y.; Zhang, B. Unveiling the Activity Origin of a Copper-based Electrocatalyst for Selective Nitrate Reduction to Ammonia. *Angew. Chem., Int. Ed.* **2020**, *59*, 5350−5354.

(27) Xu, Y.; Ren, K.; Ren, T.; Wang, M.; Liu, M.; Wang, Z.; Li, X.; Wang, L.; Wang, H. Cooperativity of Cu and Pd Active Sites in CuPd Aerogels Enhances Nitrate Electroreduction to Ammonia. *Chem. Commun.* **2021**, *57*, 7525−7528.

(28) Xu, Y.; Ren, K.; Ren, T.; Wang, M.; Wang, Z.; Li, X.; Wang, L.; Wang, H. Ultralow-content Pd in-situ Incorporation Mediated Hierarchical Defects in Corner-etched Cu_2O Octahedra for Enhanced Electrocatalytic Nitrate Reduction to Ammonia. *Appl. Catal., B* **2022**, *306*, 121094.

(29) Zheng, Y.; Qin, M.; Yu, X.; Yao, H.; Zhang, W.; Xie, G.; Guo, X. Constructing Ru@C_3N_4/Cu Tandem Electrocatalyst with Dual-active Sites for Enhanced Nitrate Electroreduction to Ammonia. *Small* **2023**, *19*, 2302266.

(30) Liu, S.; Yan, L.; Chen, Q.; Wu, B.; Zhu, H.; Zhou, S.; Wang, X.; Zhao, X.; Sun, C.; Li, Y.; Lei, L.; Li, Z.; Hou, Y.; Yang, B. Unveiling the Facet-dependent Activity of Cu_2O for Enhanced Selective Electroreduction of Nitric Oxide to Ammonia and Zn-NO Batteries. *Process Safety and Environmental Protection* **2024**, *187*, 312−319.

(31) Nugraha, A.; Ashok, A.; Xia, W.; Miyata, H. M.; Alshehri, S.; Ahamad, T.; Bando, Y.; Han, M.; Yamauchi, Y. Dealloying Strategies for Mesoporous AuCu Nanoparticles: Impact on Internal Metallic Structure and Electrocatalytic Performance. *Small Structures* **2024**, *5*, 2400021.

(32) Zhang, Z.; Zhang, N.; Zhang, J.; Deng, B.; Cao, Z.; Wang, Z.; Wei, G.; Zhang, Q.; Jia, R.; Xiang, P.; Xia, S. Critical Review in Electrocatalytic Nitrate Reduction to Ammonia Towards a Sustainable Nitrogen Utilization. *Chem. Eng. J.* **2024**, *483*, 148952.

(33) Zhao, X.; Jiang, Y.; Wang, M.; Liu, S.; Wang, Z.; Qian, T.; Yan, C. Optimizing Intermediate Adsorption Via Heteroatom Ensemble Effect over RuFe Bimetallic Alloy for Enhanced Nitrate Electroreduction to Ammonia. *Adv. Energy Mater.* **2023**, *13*, 2301409.

(34) Iarchuk, A.; Dutta, A.; Broekmann, P. Novel Ni Foam Catalysts for Sustainable Nitrate to Ammonia Electroreduction. *Journal of Hazardous Materials* **2022**, *439*, 129504.

(35) Wang, X.; Ma, X.; Wu, Y.; Li, C.; Chen, R. Electrocatalytic Nitrate Removal by Non-precious Three-dimensional Fe/Ni Foam Cathode: Experimental Study and Mechanism Verification. *Journal of Water Process Engineering* **2024**, *64*, 105590.

(36) Zheng, W.; Zhu, L.; Yan, Z.; Lin, Z.; Lei, Z.; Zhang, Y.; Xu, H.; Dang, Z.; Wei, C.; Feng, C. Self-activated Ni Cathode for Electrocatalytic Nitrate Reduction to Ammonia: From Fundamentals to Scale-up for Treatment of Industrial Wastewater. *Environ. Sci. Technol.* **2021**, *55*, 13231−13243.

(37) Li, F.; Liu, C.; Lin, H.; Sun, Y.; Yu, H.; Xue, S.; Cao, J.; Jia, X.; Chen, S. High Activity of Bifunctional Ni_2P Electrocatalyst for Benzyl Alcohol Oxidation Coupled with Hydrogen Evolution. *J. Colloid Interface Sci.* **2023**, *640*, 329−337.

(38) Crombie, C.; Lewis, R.; Taylor, R.; Morgan, D.; Davies, T.; Folli, A.; Murphy, D.; Edwards, J.; Qi, J.; Jiang, H.; Kiely, C.; Liu, X.; Skjoth-Rasmussen, M.; Hutchings, G. Enhanced Selective Oxidation of Benzyl Alcohol Via in Situ H_2O_2 Production over Supported Pd-based Catalysts. *ACS Catal.* **2021**, *11*, 2701−2714.

(39) Li, Z.; Yan, Y.; Xu, S.; Zhou, H.; Xu, M.; Ma, L.; Shao, M.; Kong, X.; Wang, B.; Zheng, L.; Duan, H. Alcohols Electrooxidation Coupled with H_2 Production at High Current Densities Promoted by a Cooperative Catalyst. *Nat. Commun.* **2022**, *13*, 147−147.

(40) Luo, L.; Wang, Z.; Xiang, X.; Yan, D.; Ye, J. Selective Activation of Benzyl Alcohol Coupled with Photoelectrochemical Water Oxidation Via a Radical Relay Strategy. *ACS Catal.* **2020**, *10*, 4906−4913.

(41) Song, J.; Yinhai, Y.; Jia, Y.; Wang, T.; Wei, J.; Wang, M.; Zhou, S.; Li, Z.; Hou, Y.; Lei, L.; Yang, B. Improved NH_3-N Conversion Efficiency to N_2 Activated by Bdd Substrate on NiCu Electrocatalysis Process. *Sep. Purif. Technol.* **2021**, *276*, 119350.

(42) Wang, J.; Feng, J.; Soyol-Erdene, T.; Wei, Z.; Tang, W. Electrodeposited NiCoP on Nickel Foam as a Self-supported Cathode for Highly Selective Electrochemical Reduction of Nitrate to Ammonia. *Sep. Purif. Technol.* **2023**, *320*, 124155.

(43) Kresse, G.; Furthmuller, J. Efficient Iterative Schemes for Ab Initio Total-energy Calculations Using a Plane-wave Basis Set. *Phys. Rev. B* **1996**, *54*, 11169−11186.

(44) Kresse, G.; Furthmuller, J. Efficiency of ab-initio Total Energy Calculations for Metals and Semiconductors Using a Plane-wave Basis Set. *Comput. Mater. Sci.* **1996**, *6*, 15−50.

(45) He, Y.; Liu, S.; Wang, M.; Ji, H.; Zhang, L.; Cheng, Q.; Qian, T.; Yan, C. Advancing the Electrochemistry of Gas-involved Reactions through Theoretical Calculations and Simulations from Microscopic to Macroscopic. *Adv. Funct. Mater.* **2022**, *32*, 2208474.

(46) Perdew, J.; Burke, K.; Ernzerhof, M. Generalized Gradient Approximation Made Simple. *Phys. Rev. Lett.* **1996**, *77*, 3865−3868.

(47) Blöchl, P.; Först, C.; Schimpl, J. Projector Augmented Wave Method: Ab Initio Molecular Dynamics with Full Wave Functions. *Bull. Mater. Sci.* **2003**, *26*, 33−41.

(48) Grimme, S.; Ehrlich, S.; Goerigk, L. Effect of the Damping Function in Dispersion Corrected Density Functional Theory. *J. Comput. Chem.* **2011**, *32*, 1456−1465.

(49) Xiong, J.; Dong, X.; Song, Y.; Dong, Y. A High Performance Ru-ZrO_2/Carbon Nanotubes-Ni Foam Composite Catalyst for Selective Co Methanation. *J. Power Sources* **2013**, *242*, 132−136.

(50) Wang, X.; Peng, X.; Ran, H.; Lin, B.; Ni, J.; Lin, J.; Jiang, L. Influence of Ru Substitution on the Properties of $LaCoO_3$ Catalysts for Ammonia Synthesis: XAFS and XPS Studies. *Ind. Eng. Chem. Res.* **2018**, *57*, 17375−17383.

(51) Fu, W.; Du, Y.; Jing, J.; Fu, C.; Zhou, M. Highly Selective Nitrate Reduction to Ammonia on CoO/Cu Foam Via Constructing Interfacial Electric Field to Tune Adsorption of Reactants. *Appl. Catal., B* **2023**, *324*, 122201.

(52) Liu, X.; Guo, R.; Qin, X.; Xu, C. Enhanced Selective Nitrate-to-nitrogen Electrocatalytic Reduction by Cnts Doped Ni Foam/Cu Electrode Coupled with Cl^-. *Journal of Water Process Engineering* **2023**, *54*, 104067.

(53) Xiao, Z.; Huang, Y.; Dong, C.; Xie, C.; Liu, Z.; Du, S.; Chen, W.; Yan, D.; Tao, L.; Shu, Z.; Zhang, G.; Duan, H.; Wang, Y.; Zou, Y.; Chen, R.; Wang, S. Operando Identification of the Dynamic Behavior of Oxygen Vacancy-rich Co_3O_4 for Oxygen Evolution Reaction. *J. Am. Chem. Soc.* **2020**, *142*, 12087−12095.

(54) Wang, Y.; Zhang, L.; Niu, Y.; Fang, D.; Wang, J.; Su, Q.; Wang, C. Boosting NH_3 Production from Nitrate Electroreduction Via Electronic Structure Engineering of Fe_3C Nanoflakes. *Green Chem.* **2021**, *23*, 7594−7608.

(55) Huo, S.; Yang, S.; Niu, Q.; Yang, F.; Song, L. Synthesis of Functional Ni_2PCC Catalyst and the Robust Performances in Hydrogen Evolution Reaction and Nitrate Reduction. *Int. J. Hydrog. Energy.* **2020**, *45*, 4015−4025.

(56) Peng, O.; Hu, Q.; Zhou, X.; Zhang, R.; Du, Y.; Li, M.; Ma, L.; Xi, S.; Fu, W.; Xu, Z.; Cheng, C.; Chen, Z.; Loh, K. Swinging Hydrogen Evolution to Nitrate Reduction Activity in Molybdenum Carbide by Ruthenium Doping. *ACS Catal.* **2022**, *12,* 15045−15055.

(57) Gao, J.; Shi, N.; Guo, X.; Li, Y.; Bi, X.; Qi, Y.; Guan, J.; Jiang, B. Electrochemically Selective Ammonia Extraction from Nitrate by Coupling Electron- and Phase- Transfer Reactions at a Three-Phase Interface. *Environ. Sci. Technol.* **2021**, *55*, 10684−10694.